



NICER Observes the Effects of an X-Ray Burst on the Accretion Environment in Aql X-1

L. Keek¹, Z. Arzoumanian², P. Bult², E. M. Cackett³ , D. Chakrabarty⁴ , J. Chenevez⁵ , A. C. Fabian⁶ , K. C. Gendreau², S. Guillot^{7,8,9} , T. Güver^{10,11} , J. Homan^{12,13} , G. K. Jaisawal⁵ , F. K. Lamb^{14,15}, R. M. Ludlam¹⁶, S. Mahmoodifar² , C. B. Markwardt² , J. M. Miller¹⁶, G. Prigozhin⁴, Y. Soong^{1,2}, T. E. Strohmayer², and M. T. Wolff¹⁷

¹ Department of Astronomy, University of Maryland, College Park, MD 20742, USA; lkeek@umd.edu

² X-ray Astrophysics Laboratory, Astrophysics Science Division, NASA/GSFC, Greenbelt, MD 20771, USA

³ Department of Physics & Astronomy, Wayne State University, 666 W. Hancock Street, Detroit, MI 48201, USA

⁴ MIT Kavli Institute for Astrophysics and Space Research, Massachusetts Institute of Technology, Cambridge, MA 02139, USA

⁵ National Space Institute, Technical University of Denmark, Elektrovej 327-328, DK-2800 Lyngby, Denmark

⁶ Institute of Astronomy, Madingley Road, Cambridge CB3 0HA, UK

⁷ Instituto de Astrofísica, Facultad de Física, Pontificia Universidad Católica de Chile, Av. Vicuña Mackenna 4860, 782-0436 Macul, Santiago, Chile

⁸ CNRS, IRAP, 9 avenue du Colonel Roche, BP 44346, F-31028 Toulouse Cedex 4, France

⁹ Université de Toulouse, CNES, UPS-OMP, F-31028 Toulouse, France

¹⁰ Department of Astronomy and Space Sciences, Science Faculty, Istanbul University, Beyazıt, 34119 Istanbul, Turkey

¹¹ Istanbul University Observatory Research and Application Center, Beyazıt, 34119 Istanbul, Turkey

¹² Eureka Scientific, Inc., 2452 Delmer Street, Oakland, CA 94602, USA

¹³ SRON, Netherlands Institute for Space Research, Sorbonnelaan 2, 3584 CA Utrecht, The Netherlands

¹⁴ Center for Theoretical Astrophysics and Department of Physics, University of Illinois at Urbana-Champaign, 1110 West Green Street, Urbana, IL 61801-3080, USA

¹⁵ Department of Astronomy, University of Illinois at Urbana-Champaign, 1002 West Green Street, Urbana, IL 61801-3074, USA

¹⁶ Department of Astronomy, University of Michigan, 1085 South University Avenue, Ann Arbor, MI 48109-1107, USA

¹⁷ Space Science Division, Naval Research Laboratory, Washington, DC 20375-5352, USA

Received 2018 January 22; revised 2018 February 15; accepted 2018 February 20; published 2018 February 28

Abstract

Accretion disks around neutron stars regularly undergo sudden strong irradiation by Type-I X-ray bursts powered by unstable thermonuclear burning on the stellar surface. We investigate the impact on the disk during one of the first X-ray burst observations with the *Neutron Star Interior Composition Explorer* (NICER) on the International Space Station. The burst is seen from Aql X-1 during the hard spectral state. In addition to thermal emission from the neutron star, the burst spectrum exhibits an excess of soft X-ray photons below 1 keV, where NICER's sensitivity peaks. We interpret the excess as a combination of reprocessing by the strongly photoionized disk and enhancement of the pre-burst persistent flux, possibly due to Poynting–Robertson drag or coronal reprocessing. This is the first such detection for a short sub-Eddington burst. As these bursts are observed frequently, NICER will be able to study how X-ray bursts affect the disk and corona for a range of accreting neutron star systems and disk states.

Key words: accretion, accretion disks – stars: individual (Aql X-1) – stars: neutron – X-rays: binaries – X-rays: bursts

1. Introduction

In 2017 June, the *Neutron Star Interior Composition Explorer* (NICER; Gendreau & Arzoumanian 2017) was installed on the International Space Station. Among its first observations were two Type-I X-ray bursts from the low-mass X-ray binary Aquila X-1. X-ray bursts are known from over 100 such systems in our Galaxy, where hydrogen- and helium-rich material is accreted from a companion star onto a neutron star (for a recent review, see Galloway & Keek 2017). Runaway thermonuclear fusion of the accreted matter powers a brief (typically 10–100 s) X-ray flash during which the neutron star outshines the inner regions of the accretion disk. Sudden strong irradiation can have a multitude of effects on the disk (Ballantyne & Everett 2005), but it has been challenging to detect changes in the accretion environment because the majority of burst observations have constrained only the thermal emission from the neutron star (e.g., Swank et al. 1977; Galloway et al. 2008).

Most burst observations have been performed with instruments that are sensitive to photon energies above ~ 3 keV, such as the Proportional Counter Array (PCA; Jahoda et al. 2006) on the *Rossi X-ray Timing Explorer* (RXTE; Bradt et al. 1993).

The burst spectra are usually fit with a thermal (blackbody) component in addition to a constant “persistent” component. The latter describes the X-ray emission from accretion processes as measured outside of the burst and is assumed to remain unchanged during the burst. Deviations from the burst spectral model are found when considering a large sample of observations with RXTE/PCA (Worpel et al. 2013, 2015), which may indicate reprocessing of the burst emission or enhancement of the accretion flow due to the burst's radiation drag on the disk (Poynting–Robertson drag; e.g., Walker 1992; Miller & Lamb 1993; Lamb & Miller 1995), and a deficit of photons at >30 keV during the bursts suggests coronal cooling (Maccarone & Coppi 2003; Chen et al. 2012, 2013; Ji et al. 2014; Kajava et al. 2017). Furthermore, hours-long superbursts exhibit an iron emission line and absorption edge produced by reprocessing of the burst by the inner disk (e.g., Ballantyne 2004). Often collectively referred to as “reflection,” reprocessing involves both scattering and absorption/re-emission by the disk. The shape of the reflection spectrum depends on the ionization of the metals in the disk and on its inner radius, R_{in} , because relativistic Doppler broadening is stronger close to the neutron star. The two superbursts seen by RXTE/PCA strongly ionized the disk and

temporarily disrupted the inner disk (Ballantyne & Strohmayer 2004; Keek et al. 2014).

Most bursts are too short to enable detection of the iron line. Further reflection features are predicted in the soft X-ray band below 3 keV, including a multitude of emission lines on top of a free-free continuum (Ballantyne 2004). Burst reflection may, therefore, explain the soft excess over a blackbody detected during a bright burst observed with both *Chandra* and *RXTE*/PCA (in't Zand et al. 2013) and two long bursts seen with the *Swift* X-ray Telescope (Degenaar et al. 2013; Keek et al. 2017). Moreover, an increase of the persistent emission may also contribute to the soft excess.

NICER combines a 0.2–12 keV passband with high throughput and provides a substantially larger effective area around 1 keV than previous missions. It offers the exciting opportunity to study reflection and other signatures of burst-disk interaction even during short bursts. In this Letter, we investigate one of *NICER*'s first X-ray burst observations: a bright burst from Aql X-1. This source exhibits frequent accretion outbursts during which X-ray bursts have been observed (Koyama et al. 1981), and disk reflection has been detected in the persistent emission (King et al. 2016; Ludlam et al. 2017). After describing the *NICER* observations of Aql X-1 (Section 2), we perform a detailed analysis of the soft excess in the burst spectrum (Section 3). We discuss how an enhanced persistent component and disk reflection contribute (Section 4) and conclude that *NICER*'s ability to detect burst-disk interaction in short bursts enables investigations for a wide range of sources and spectral states.

2. Observations

NICER's X-ray Timing Instrument (XTI; Gendreau et al. 2016) consists of 56 co-aligned X-ray concentrator optics each paired with a silicon-drift detector (Prigozhin et al. 2012). The XTI provides a peak effective collecting area of 1900 cm² and a <100 eV energy resolution at 1.5 keV. In the interval 2017 June 20–July 3, *NICER* collected with 52 functioning detectors a total good exposure of 51 ks on Aql X-1 during a hard-state accretion outburst. Two Type-I bursts were observed: one in ObsID 0050340108 at MJD 57936.58042 with a peak rate of 2248 cs⁻¹ and another in ObsID 0050340109 at MJD 57937.61102 peaking at 3228 cs⁻¹. Neither burst shows significant oscillations near the neutron star's 550 Hz spin frequency (Zhang et al. 1998).

In this Letter, we analyze the brighter of the two bursts (Figure 1; the other suffers from a high particle background). During its observation the instrument pointing was accurate and stable. The ISS was on the nightside of the Earth, and the Moon was not near the pointing direction, such that optical loading effects were not significant. The ISS was not near the high particle background region of the South Atlantic Anomaly. By virtue of *NICER*'s modularity, dead time and pile-up are not an issue even at the burst peak. We process and analyze the data using HEASOFT version 6.22.1, NICERDAS 2017-09-06_V002, XSPEC 12.9.1p (Arnaud 1996) and version 0.06 of the *NICER* response files. Gain is calibrated separately for each detector. As a measure of the cosmic and instrument background, we create a spectrum from a 1117 s blank-field observation of *RXTE* background region 5 (Jahoda et al. 2006), which was also obtained at night. The count rate as a function of energy is <1 cs⁻¹ keV⁻¹, such that our observations of Aql X-1 are strongly source dominated at all energies

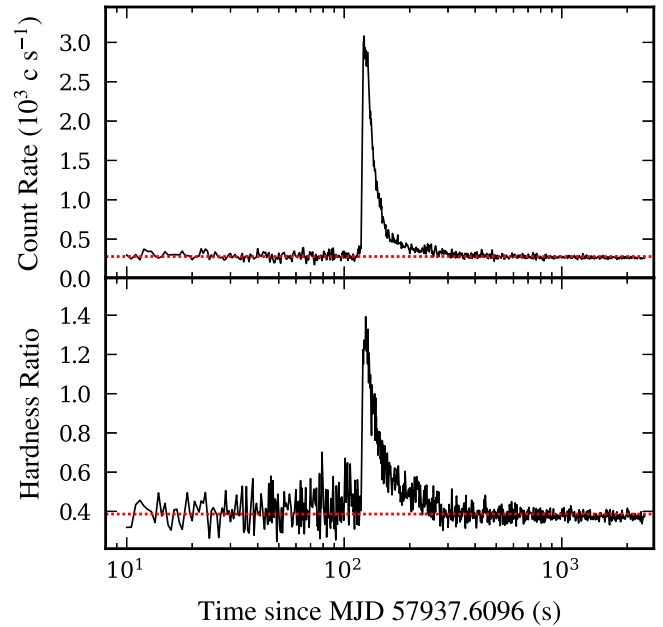


Figure 1. (Top) Light curve of the *NICER* pointing with the burst on 2017 July 3. Initially, the plotted resolution is 0.5 s, and 500 logarithmically spaced bins are employed after 150 s. (Bottom) Hardness ratio of count rate with $E > 2.5$ keV to $E < 2.5$ keV. The dotted lines indicate mean values over the first 100 s.

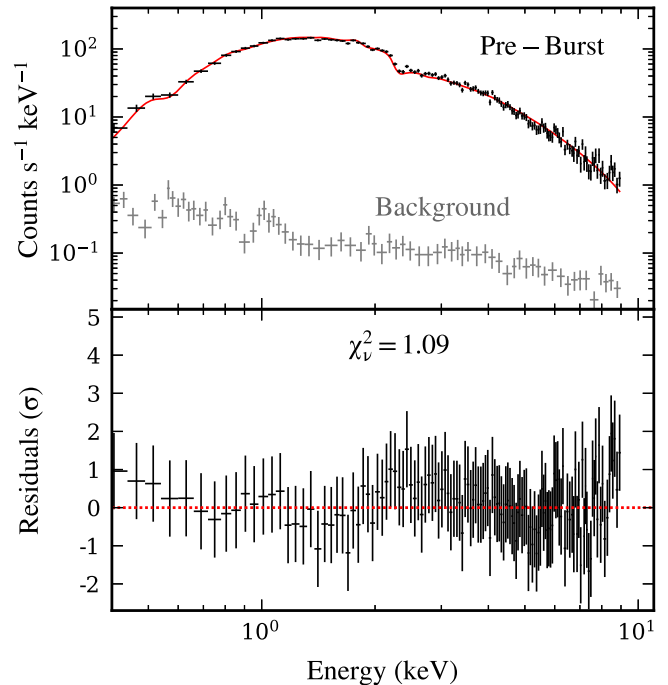


Figure 2. Spectral fit to the pre-burst spectrum as a function of energy, E . Top: pre-burst spectrum and best-fitting absorbed bremsstrahlung model (solid line). The background (rebinbed) is small with respect to the source at all energies and has been subtracted from the shown pre-burst spectrum. The absorption edge near 2.3 keV is instrumental. Bottom: fit residuals and the goodness of fit, χ^2_ν .

(Figure 2). In the source spectra, we group neighboring spectral bins with fewer than 15 counts, and in our figures, we rebin the spectra to a bin width of at least 50 eV (*NICER* data oversample the detector resolution).

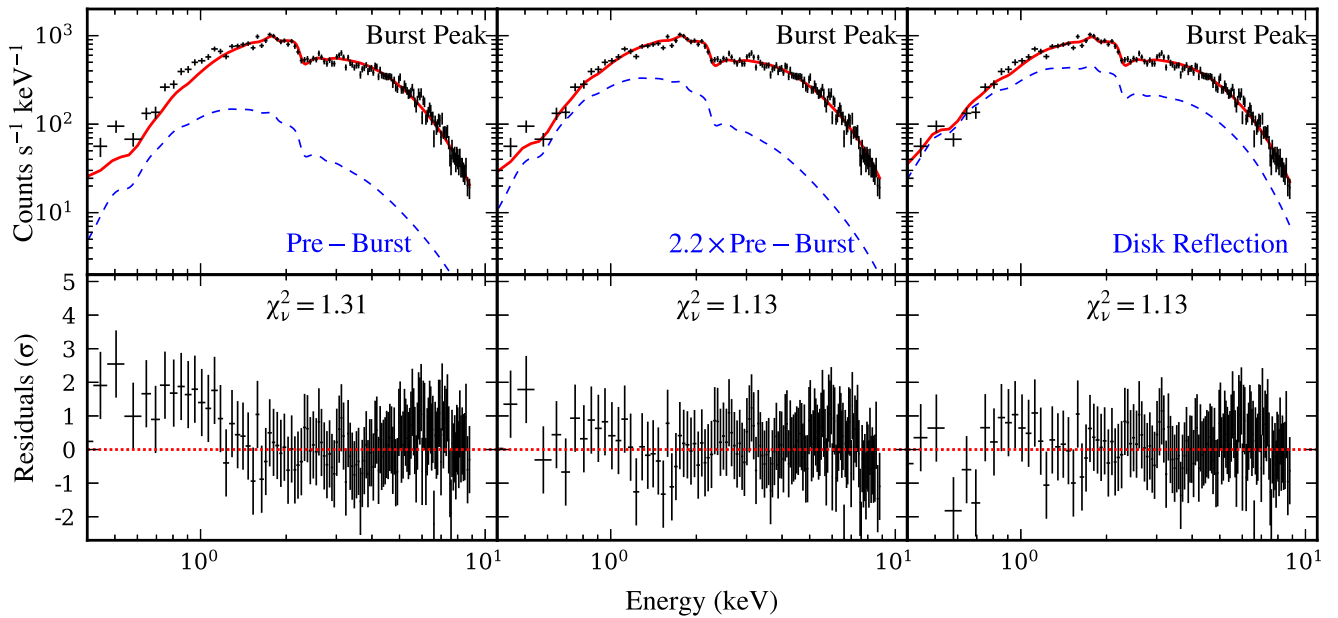


Figure 3. Spectral fits to burst peak (top panels; solid line is the best-fit model and dashed line illustrates one model component) and the fit residuals with the goodness of fit, χ^2_ν (bottom panels). Left: the commonly used spectral model with a blackbody and fixed pre-burst spectrum leaves a substantial soft excess. Middle: an increase in the normalization of the pre-burst component fits the excess. Right: alternatively, a disk reflection component produces a similar improvement.

3. Results

We analyze the spectra of the persistent emission prior to the burst and of the burst itself, looking for signatures of the impact of the burst on the accretion environment.

3.1. Pre-burst Emission

The burst occurred near the pointing’s onset, and the source does not exhibit variability outside the burst (Figure 1). We analyze the pre-burst persistent emission from a 102 s interval. We limit the analysis to the 0.3–9.0 keV band to avoid potential noise at both ends of the passband. The spectrum is well described by a thermal bremsstrahlung model (*bremss* in XSPEC; e.g., Czerny et al. 1987). More complex models (e.g., Ludlam et al. 2017) require a longer exposure to constrain their parameters, whereas our primary need is a simple description of the persistent spectrum. Interstellar absorption is modeled using the Tübingen–Boulder model (*TBabs*) with abundances from Wilms et al. (2000). With a goodness of fit of $\chi^2_\nu = 1.09$ for $\nu = 514$ degrees of freedom, the best-fitting plasma temperature is $kT = 31 \pm 4$ keV, the unabsorbed in-band flux is $(1.66 \pm 0.02) \times 10^{-9}$ erg s $^{-1}$ cm $^{-2}$, and the absorption column is $N_H = (5.39 \pm 0.09) \times 10^{21}$ cm $^{-2}$ (1σ uncertainties).

Extrapolating the bremsstrahlung model over the 0.001–100 keV range, we find an unabsorbed bolometric flux of $F_{\text{pre-burst}} = (4.3 \pm 0.3) \times 10^{-9}$ erg s $^{-1}$ cm $^{-2}$. We compare it to the peak fluxes of Eddington-limited bursts from Aql X-1 observed with *RXTE*/PCA: $F_{\text{Edd}} = (1.0 \pm 0.2) \times 10^{-7}$ erg s $^{-1}$ cm $^{-2}$ (Worpel et al. 2015). The pre-burst flux level is, therefore, $\sim 5\% F_{\text{Edd}}$.

The value of N_H is well within the range derived from observations of the source with the *XMM-Newton*, *Chandra*, and *Swift* observatories (e.g., Campana et al. 2014). N_H measurements from radio and infrared maps of Galactic hydrogen¹⁸ (Schlegel et al. 1998; Kalberla et al. 2005;

Willingale et al. 2013) find within 1° of the source $N_H = 4.30 \times 10^{21}$ cm $^{-2}$, which is 20% lower than our value. Because the difference is modest, we use our value in the burst analysis for consistency.

3.2. Burst Peak

We extract a spectrum around the time when the flux peaks (Figure 3) during a 6 s interval (starting at 2.3 s in Figure 4). First, we employ the commonly used spectral model for bursts: we keep the parameters of the pre-burst spectrum fixed, and we add an absorbed blackbody (*bbbodyrad*) component to model the thermal emission from the burst. When left free, the best-fitting value of N_H is substantially smaller than both the pre-burst fit and the Galactic hydrogen maps indicate. Similar to Keek et al. (2017), we fix N_H to the pre-burst value: the fit yields $\chi^2_\nu = 1.31$ ($\nu = 560$), and a substantial soft excess is visible in the fit residuals below $E \lesssim 1$ keV (Figure 3, left). At 0.8 keV, the observed count rate is ~ 2 times the value of the best-fitting blackbody model, and the excess is ~ 500 times the background.

We investigate two interpretations of the soft excess. Following Worpel et al. (2013) we include a multiplication factor, f_a , for the normalization of the bremsstrahlung component. We find a best-fitting value of $f_a = 2.24 \pm 0.13$. The fit is improved ($\chi^2_\nu = 1.13$, $\nu = 559$), and the soft excess is largely removed from the residuals (Figure 3, middle). Comparing this fit to the previous fit with an F-test indicates a significant improvement with a null-hypothesis probability of 5×10^{-20} .

Alternatively, the excess may result from reprocessing by the disk. We employ the burst reflection model that was successfully applied to the two *RXTE*/PCA superbursts (Ballantyne 2004; Ballantyne & Strohmayer 2004; Keek et al. 2014), which consists of a table of detailed reflection spectra calculated for blackbody illumination of a (in this case, solar-composition) disk. A reflection component is added to our spectral model, and the absorption and bremsstrahlung

¹⁸ See <http://www.swift.ac.uk/analysis/nhtot/>.

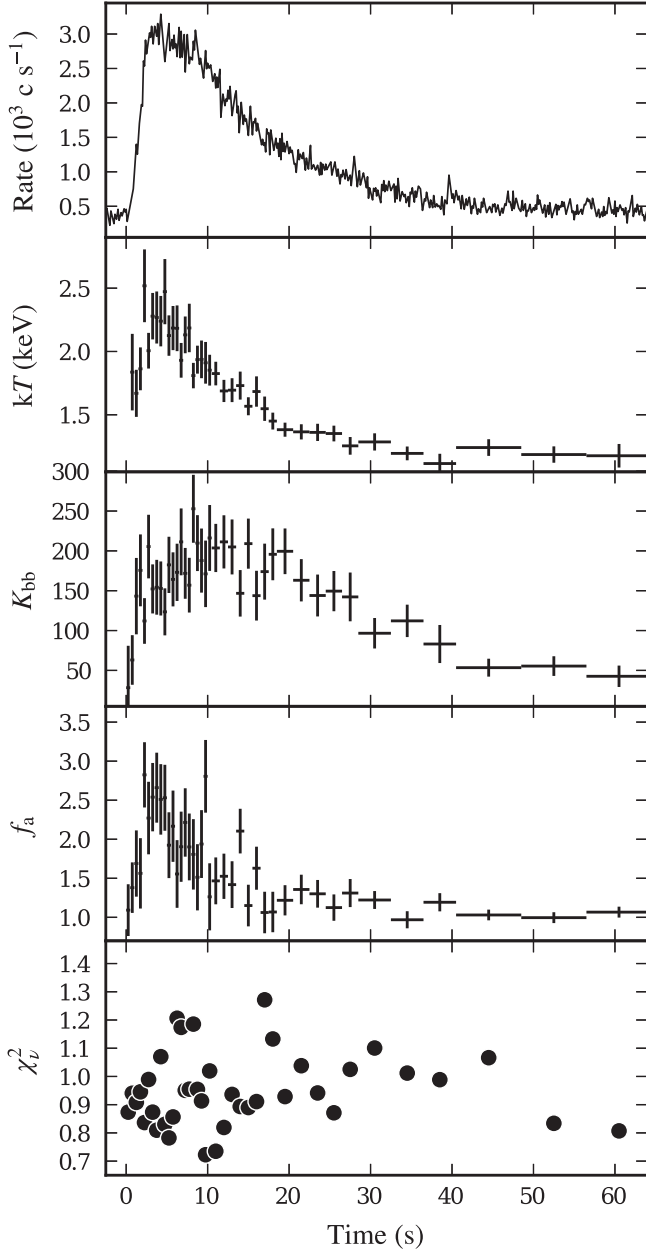


Figure 4. Time-resolved spectroscopy with a model that includes a scaled pre-burst component. Top panel: count rate in the full passband at 1/8 s resolution. Other panels show the best-fit values for the blackbody temperature, kT , and normalization, K_{bb} , as well as the scaling factor of the pre-burst component, f_a . Horizontal bars indicate the width of the time bins, and vertical bars are the 1σ uncertainties. The bottom panel presents the goodness of fit per degree of freedom, χ^2_ν .

parameters are kept fixed. Relativistic Doppler broadening of the reflection component is modeled with the `rdblur` convolution model (Fabian et al. 1989), using an emissivity profile that drops off with the third power of the disk radius and assuming a disk inclination angle of 20° (King et al. 2016). We find a similar significant improvement in the fit as with the f_a model: $\chi^2_\nu = 1.13$ ($\nu = 557$; Figure 3, right). The reflection fraction (the flux ratio of the reflection to blackbody component) is $f_{\text{refl}} = 0.37 \pm 0.05$. As no discrete features such as lines are visible, the fit prefers the largest values of the ionization parameter in our table model, $\log \xi = 3.66^{+p}_{-0.11}$, where “ p ” indicates that the search for the 1σ confidence region

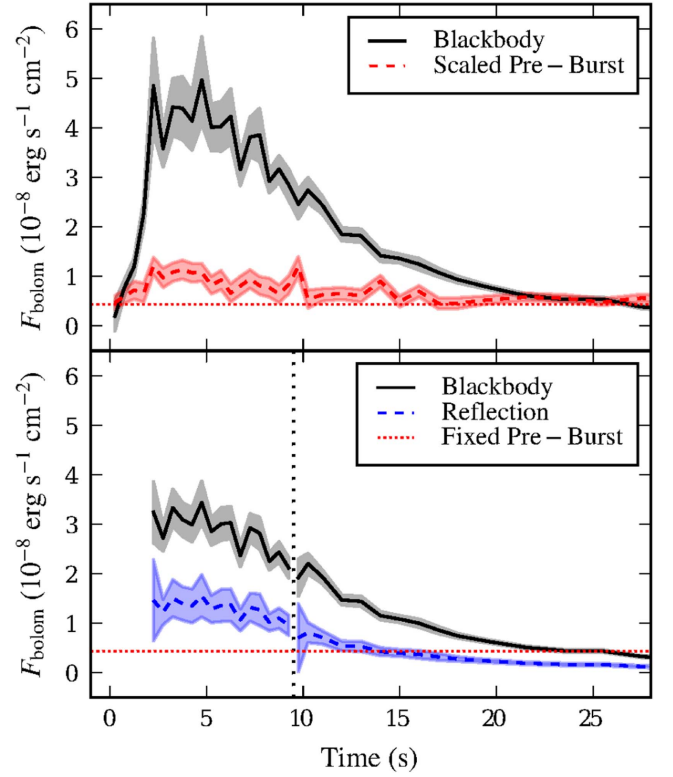


Figure 5. Bolometric unabsorbed flux from time-resolved spectroscopy, where the shaded bands indicate the 1σ error regions. Top: fit with scaled pre-burst component shows this part to increase during the burst (dotted line indicates the pre-burst flux level). Bottom: alternative fit with reflection model. The vertical dotted line demarcates the two fitted intervals of the peak and tail.

is pegged at the table boundary of $\log \xi = 3.75$. For similar reasons, the fit prefers the strongest broadening, which is given by an inner disk radius of $R_{\text{in}} = 6 R_g$ ($R_g = GM/c^2$ is the gravitational radius), but this parameter is not strongly constrained.

3.3. Time-resolved Spectroscopy

We analyzed a 6 s time interval around the peak, but the spectral parameters evolve on shorter timescales, requiring time-resolved spectroscopy. We divide the burst into intervals of 0.5 s at the burst onset, and after the peak we double the duration each time the count rate drops by another factor of $\sqrt{2}$, such that we have similar statistics throughout the burst. We analyze the first minute of the burst where the parameters of two spectral components can be constrained, although the tail of the burst is detected for another ~ 120 s due to *NICER*’s soft-band sensitivity to declining temperatures (Figure 1).

First, we fit the f_a model. f_a increases at the burst onset to a maximum, and returns to 1 in the tail (Figure 4). In seven bins around the peak, the weighted mean is $f_a = 2.5 \pm 0.2$. We use the XSPEC model `cflux` to determine the unabsorbed bolometric flux of the spectral components (Figure 5, top). The flux of the scaled pre-burst component, F_{bremss} , follows the blackbody flux, F_{bb} : a linear fit to the first 15 s of the burst yields $F_{\text{bremss}} = F_{\text{pre-burst}} + (0.128 \pm 0.012)F_{bb}$ ($\chi^2_\nu = 0.83$, $\nu = 24$), where $F_{\text{pre-burst}}$ is the persistent flux from Section 3.1.

Next, we repeat the time-resolved fits with the reflection model. This model includes more parameters, which are hard to constrain within short time intervals. Because R_{in} was weakly

constrained in Section 3.2, we fix its value to $R_{\text{in}} = 15 R_g$, inferred from reflection spectroscopy of the persistent emission in the soft state of Aql X-1 (King et al. 2016). An updated analysis of the soft state (Ludlam et al. 2017) and a study of the hard state (Sakurai et al. 2012) reveal similar R_{in} , and our burst results are insensitive to the differences. A preliminary investigation of the persistent emission from all *NICER* data on Aql X-1 shows a broad Fe line similar in shape to that seen with *NuSTAR* during the soft state (Ludlam et al. 2017), supporting our choice of R_{in} . Furthermore, we limit the fit to the spectra in an 8 s interval around the peak (starting at 2 s in Figure 4), where we can reasonably expect $\log \xi$ to be large. We fit all spectra in that interval simultaneously, assuming $\log \xi$ and f_{refl} to be the same everywhere, and kT is fit for each spectrum. We find $\log \xi = 3.75^{+p}_{-0.2}$ and $f_{\text{refl}} = 0.45 \pm 0.08$ ($\chi^2_\nu = 0.93$ with $\nu = 1244$). kT is consistent within 1σ with the values from the fit with the f_a model (Figure 4). Immediately following this time interval, we repeat this exercise for the tail of the burst, obtaining $\log \xi = 3.75^{+p}_{-0.2}$ and $f_{\text{refl}} = 0.37 \pm 0.11$ ($\chi^2_\nu = 0.95$ with $\nu = 1731$), which are consistent with the values around the peak. The blackbody flux is lower than for the f_a model (Figure 5) because the reflection model also contributes to the thermal continuum.

In seven bins around the peak, the weighted mean of the bolometric unabsorbed blackbody flux is $F_{\text{bb}} = (4.1 \pm 0.2) \times 10^{-8} \text{ erg s}^{-1} \text{ cm}^{-2}$ for the f_a model and $F_{\text{bb}} = (2.7 \pm 0.4) \times 10^{-8} \text{ erg s}^{-1} \text{ cm}^{-2}$ for the reflection model ($F = (4.2 \pm 0.2) \times 10^{-8} \text{ erg s}^{-1} \text{ cm}^{-2}$ including the reflection component), which is $\sim 40\%$ F_{Edd} (Section 3.1). The bolometric flux at the peak of all components combined (including pre-burst for the reflection fit) is $F_{\text{total}} = (5.1 \pm 0.3) \times 10^{-8} \text{ erg s}^{-1} \text{ cm}^{-2}$ for the f_a model and $F_{\text{total}} = (4.8 \pm 0.2) \times 10^{-8} \text{ erg s}^{-1} \text{ cm}^{-2}$ for the reflection model, which are consistent within 1σ .

4. Discussion

We find that both an enhanced persistent component and disk reflection can explain the soft excess detected by *NICER* in a burst from Aql X-1. Other interpretations may be possible. For example, free-free absorption in the neutron star atmosphere could produce a soft excess (e.g., Suleimanov et al. 2012). However, we find that fits with atmosphere models are unable to explain the full soft excess, whereas reflection and enhanced persistent emission were found to be important for the interpretation of, e.g., the superbursts seen with *RXTE/PCA* (Ballantyne & Strohmayer 2004; Keek et al. 2014). Here, we discuss how these two components can provide a consistent physical picture of the impact of the burst.

4.1. Enhanced Persistent Emission

The f_a model scales the persistent flux prior to the burst. The peak value of $f_a = 2.5 \pm 0.2$ is typical for bursts without photospheric expansion at a similar persistent flux (Worpel et al. 2015). Worpel et al. (2015) used *RXTE/PCA* spectra, which do not cover the soft band $E \lesssim 3 \text{ keV}$, and it is therefore interesting that we obtain a roughly similar value. We find that the increase in the persistent flux is proportional to the blackbody flux, suggesting that the increase is caused by burst irradiation. It is possible that radiation drag enhances accretion during the burst (Worpel et al. 2013). Alternatively, the soft excess may be produced by reprocessing of the burst flux in an

optically thin medium such as the corona. *RXTE/PCA* observations of similar bursts from Aql X-1 in the hard state exhibit a substantial flux decrease in the 40–50 keV band, possibly caused by coronal cooling induced by the burst (Chen et al. 2013). The simplistic f_a model does not probe this temperature evolution, and the application of physically better motivated models requires broadband observations with *NICER* and *NuSTAR* or *ASTROSAT*.

4.2. Disk Reflection

The soft excess could also be produced by reprocessing on the disk (Ballantyne 2004). For a highly ionized disk, the fluorescent Fe $K\alpha$ line from reflection is challenging to detect during a burst with *NICER*, whereas the soft excess is highly significant (Keek et al. 2016). For an inclination angle of 20° (King et al. 2016) the expected reflection fraction is $f_{\text{refl}} = 0.52$ for a thin disk that extends to the neutron star (He & Keek 2016). The disk has, however, been observed to truncate at $R_{\text{in}} \simeq 15 R_g$ (Sakurai et al. 2012; King et al. 2016). From Figure 5 in He & Keek (2016) we estimate that for a $1.4 M_\odot$ and 10 km radius neutron star this gap reduces the reflection fraction to $f_{\text{refl}} \simeq 0.15$. We find triple this value, $f_{\text{refl}} = 0.45 \pm 0.08$, for the burst. If one assumes that the burst does not change the disk geometry, only 1/3 of the soft excess is due to reflection, and the rest could result from an enhancement of the persistent flux. To produce $f_{\text{refl}} = 0.45$, the impact of the burst must have caused the inner disk to (temporarily) extend close to the neutron star surface. A similar suggestion was made for the long burst from IGR J17062–6143 (Keek et al. 2017).

The intermittent presence of dips observed from Aql X-1 may hint at a larger inclination angle of $\sim 75^\circ$ (Galloway et al. 2016). At this angle, $f_{\text{refl}} = 0.10$ is expected when the disk extends to the stellar surface (He & Keek 2016), and $f_{\text{refl}} = 0.03$ for $R_{\text{in}} \simeq 15 R_g$. Under these assumptions, reflection contributes only a small part of the soft excess detected by *NICER*.

Unfortunately, we could not track R_{in} during the burst from the reflection signal. This may require the analysis of a larger sample of bursts, a superburst observation with *NICER*, or a future mission with even larger collecting area such as *STROBE-X* (Wilson-Hodge et al. 2017).












5. Conclusions and Outlook

One of *NICER*'s first X-ray burst observations was a sub-Eddington burst from Aql X-1 in the hard state. The spectrum exhibits a soft excess over the thermal burst emission, which can be explained by either enhanced persistent (accretion) emission or disk reflection. From the known disk truncation radius, we expect at least a third of the excess to be disk reflection. For reflection to produce all of the excess, burst irradiation must cause the inner disk to temporarily move close to the stellar surface. Alternatively, the excess may be powered by Poynting–Robertson drag or coronal reprocessing. Regardless of the precise interpretation, this demonstrates that bursts have a substantial impact on their accretion environment, even in the hard spectral state, which is preferred for neutron star mass–radius measurements (e.g., Kajava et al. 2014). Whereas previously this was only detectable in rare cases or by considering large samples, a preliminary analysis of *NICER* burst observations finds the soft excess in a number of short

bursts. This will allow us to study the burst–disk interaction across multiple sources and spectral states, mapping out how bursts impact different accretion geometries.

This work was supported by NASA through the *NICER* mission and the Astrophysics Explorers Program. It benefited from JINA CEE (NSF grant PHY-1430152). E.M.C. acknowledges NSF CAREER award AST-1351222. S.G. acknowledges CNES.

ORCID iDs

E. M. Cackett  <https://orcid.org/0000-0002-8294-9281>
D. Chakrabarty  <https://orcid.org/0000-0001-8804-8946>
J. Chenevez  <https://orcid.org/0000-0002-4397-8370>
A. C. Fabian  <https://orcid.org/0000-0002-9378-4072>
S. Guillot  <https://orcid.org/0000-0002-6449-106X>
T. Güver  <https://orcid.org/0000-0002-3531-9842>
J. Homan  <https://orcid.org/0000-0001-8371-2713>
G. K. Jaisawal  <https://orcid.org/0000-0002-6789-2723>
S. Mahmoodifar  <https://orcid.org/0000-0003-2386-1359>
C. B. Markwardt  <https://orcid.org/0000-0001-9803-3879>
M. T. Wolff  <https://orcid.org/0000-0002-4013-5650>

References

- Arnaud, K. A. 1996, in ASP Conf. Ser. 101, *Astronomical Data Analysis Software and Systems V*, ed. G. H. Jacoby & J. Barnes (San Francisco, CA: ASP), 17
- Ballantyne, D. R. 2004, *MNRAS*, 351, 57
- Ballantyne, D. R., & Everett, J. E. 2005, *ApJ*, 626, 364
- Ballantyne, D. R., & Strohmayer, T. E. 2004, *ApJL*, 602, L105
- Bradt, H. V., Rothschild, R. E., & Swank, J. H. 1993, *A&AS*, 97, 355
- Campana, S., Brivio, F., Degenaar, N., et al. 2014, *MNRAS*, 441, 1984
- Chen, Y.-P., Zhang, S., Zhang, S.-N., et al. 2013, *ApJL*, 777, L9
- Chen, Y.-P., Zhang, S., Zhang, S.-N., Li, J., & Wang, J.-M. 2012, *ApJL*, 752, L34
- Czerny, M., Czerny, B., & Grindlay, J. E. 1987, *ApJ*, 312, 122
- Degenaar, N., Miller, J. M., Wijnands, R., Altamirano, D., & Fabian, A. C. 2013, *ApJL*, 767, L37
- Fabian, A. C., Rees, M. J., Stella, L., & White, N. E. 1989, *MNRAS*, 238, 729
- Galloway, D. K., Ajamyan, A. N., Upjohn, J., & Stuart, M. 2016, *MNRAS*, 461, 3847
- Galloway, D. K., & Keek, L. 2017, arXiv:1712.06227
- Galloway, D. K., Munro, M. P., Hartman, J. M., Psaltis, D., & Chakrabarty, D. 2008, *ApJS*, 179, 360
- Gendreau, K., & Arzoumanian, Z. 2017, *NatAs*, 1, 895
- Gendreau, K. C., Arzoumanian, Z., Adkins, P. W., et al. 2016, *Proc. SPIE*, 9905, 99051H
- He, C.-C., & Keek, L. 2016, *ApJ*, 819, 47
- in't Zand, J. J. M., Galloway, D. K., Marshall, H. L., et al. 2013, *A&A*, 553, A83
- Jahoda, K., Markwardt, C. B., Radeva, Y., et al. 2006, *ApJS*, 163, 401
- Ji, L., Zhang, S., Chen, Y., et al. 2014, *ApJ*, 782, 40
- Kajava, J. J. E., Sánchez-Fernández, C., Kuulkers, E., & Poutanen, J. 2017, *A&A*, 599, A89
- Kajava, J. J. E., Nättälä, J., Latvala, O.-M., et al. 2014, *MNRAS*, 445, 4218
- Kalberla, P. M. W., Burton, W. B., Hartmann, D., et al. 2005, *A&A*, 440, 775
- Keek, L., Ballantyne, D. R., Kuulkers, E., & Strohmayer, T. E. 2014, *ApJL*, 797, L23
- Keek, L., Iwakiri, W., Serino, M., et al. 2017, *ApJ*, 836, 111
- Keek, L., Wolf, Z., & Ballantyne, D. R. 2016, *ApJ*, 826, 79
- King, A. L., Tomsick, J. A., Miller, J. M., et al. 2016, *ApJL*, 819, L29
- Koyama, K., Inoue, H., Makishima, K., et al. 1981, *ApJL*, 247, L27
- Lamb, F. K., & Miller, M. C. 1995, *ApJ*, 439, 828
- Ludlam, R. M., Miller, J. M., Degenaar, N., et al. 2017, *ApJ*, 847, 135
- Maccarone, T. J., & Coppi, P. S. 2003, *A&A*, 399, 1151
- Miller, M. C., & Lamb, F. K. 1993, *ApJL*, 413, L43
- Prigozhin, G., Gendreau, K., Foster, R., et al. 2012, *Proc. SPIE*, 8453, 845318
- Sakurai, S., Yamada, S., Torii, S., et al. 2012, *PASJ*, 64, 72
- Schlegel, D. J., Finkbeiner, D. P., & Davis, M. 1998, *ApJ*, 500, 525
- Suleimanov, V., Poutanen, J., & Werner, K. 2012, *A&A*, 545, A120
- Swank, J. H., Becker, R. H., Boldt, E. A., et al. 1977, *ApJL*, 212, L73
- Walker, M. A. 1992, *ApJ*, 385, 642
- Willingale, R., Starling, R. L. C., Beardmore, A. P., Tanvir, N. R., & O'Brien, P. T. 2013, *MNRAS*, 431, 394
- Wilms, J., Allen, A., & McCray, R. 2000, *ApJ*, 542, 914
- Wilson-Hodge, C. A., Ray, P. S., Gendreau, K., et al. 2017, *ResPh*, 7, 3704
- Worpel, H., Galloway, D. K., & Price, D. J. 2013, *ApJ*, 772, 94
- Worpel, H., Galloway, D. K., & Price, D. J. 2015, *ApJ*, 801, 60
- Zhang, W., Jahoda, K., Kelley, R. L., et al. 1998, *ApJL*, 495, L9